ELSEVIER

Earth and Planetary Science Letters 154 (1998) 53–71

EPSL

The composition of peridotites and their minerals: a laser-ablation ICP–MS study

S.M. Eggins [1], R.L. Rudnick [*], W.F. McDonough [2]

Research School of Earth Sciences, The Australian National University, Canberra, ACT 0200, Australia

Received 14 February 1997; revised 26 August 1997; accepted 3 October 1997

Abstract

We have analyzed the major- and trace-element contents of minerals and whole rocks for two peridotite xenoliths from SE Australia (one fertile, the other infertile) using both solution chemistry (ICP–MS) and microbeam techniques (EMP, LA–ICP–MS). The incompatible lithophile trace elements are contained mainly in solid mineral phases at upper-mantle conditions, with no significant concentrations occurring on grain boundaries or in fluid inclusions. No exotic accessory minerals are required hosts for elements such as Nb and Ta. Mass balance is achieved for the highly incompatible trace elements only with inclusion of data for precursor amphibole, now present as pockets of alkali-, alumina- and silica-rich glass containing euhedral olivine, clinopyroxene, and spinel daughter crystals. The glass in these pockets is enriched in incompatible trace elements, particularly Ba, Nb and Ta, reflecting the preferential partitioning of these elements into amphibole at upper-mantle conditions. Orthopyroxene–clinopyroxene partition coefficients are similar for most incompatible elements (except Ti) between the two peridotites, suggesting that compositional differences do not significantly affect subsolidus partitioning for these elements. Comparison of our data with those from the literature reveals large variations in $D^{opx/cpx}$ for all incompatible trace elements. For the REE, Zr (Hf) and Sr, these variations correlate with reciprocal equilibration temperature, reflecting the substitution of these elements for Ca in the M2 site. In contrast, poor correlation exists for V and no correlations exist for Ti and Nb between $D^{opx/cpx}$ and temperature, which may reflect their substitution into multiple sites in the pyroxene structure and the influence of mineral composition on their partitioning. These features highlight the need for caution in inferring crystal–liquid *D*-values from subsolidus partitioning relations. © 1998 Elsevier Science B.V.

Keywords: peridotites; trace-element analyses; partition coefficient; inductively coupled plasma methods

1. Introduction

Studies of the abundance and distribution of elements in peridotites and their constituent minerals are important for understanding the chemical evolution and composition of the lithospheric mantle, as well as other parts of the upper mantle and the silicate earth. Such studies allow us to characterize the subsolidus distribution of elements between coexisting minerals and to constrain the composition of

[*] Corresponding author. Present address: Department of Earth and Planetary Sciences, Harvard University, 20 Oxford Street, Cambridge, MA 02174, USA. E-mail: rudnick@eps.harvard.edu

[1] Present address: Department of Geology, The Australian National University, Canberra, ACT 0200, Australia. E-mail: stephen.eggins@anu.edu.au

[2] Present address: Department of Earth and Planetary Sciences, Harvard University, 20 Oxford Street, Cambridge, MA 02174, USA. E-mail: mcdonough.@eps.harvard.edu

0012-821X/98/$19.00 © 1998 Elsevier Science B.V. All rights reserved.
PII S0012-821X(97)00195-7

the upper mantle. When combined with thermobarometric data, the subsolidus distribution data provide further understanding of the temperature and pressure dependence of element partitioning between upper-mantle phases.

The pioneering studies of Frey [1], Nagasawa et al. [2], Frey and Green [3], and Shimizu [4] established the first-order distribution of major and trace elements between peridotite minerals under upper-mantle conditions. Their work established that the bulk of the rare-earth elements (REE) are hosted in clinopyroxene and garnet (when present) with orthopyroxene playing a minor role in the REE budget. Subsequent microbeam studies by Shimizu and colleagues [5–9] provided new insights into the relative distribution of other incompatible trace elements, in addition to the REE, between silicate minerals in mantle peridotites. We have now reached a new

Table 1
Major-element compositions of bulk peridotites and their minerals

2905	ol	± [a]	opx	±	cpx	±	sp	±	Glass[b]	±	Bulk rock	
Mode %[c]	59.9		24.2		13.7		1.9		0.6		measured	calculated
SiO_2	40.79	0.10	55.06	0.14	52.79	0.21			55.5	1.28	45.10	45.14
TiO_2	0.006	0.003	0.12	0.01	0.45	0.02			2.29	0.24	0.11	0.10
Al_2O_3			4.74	0.10	6.68	0.13	57.41	0.11	21.2	0.20	3.13	3.17
Cr_2O_3	0.01		0.37	0.02	0.74	0.04	11.51	0.11			0.44	0.42
FeO	9.44	0.11	5.97	0.05	2.72	0.04	10.74	0.08	3.23	0.16	7.59	7.69
MnO	0.16	0.02	0.17	0.02	0.12	0.01					0.12	0.15
NiO	0.39	0.02	0.15	0.01	0.05	0.001					0.27	0.28
MgO	49.14	0.05	32.62	0.13	15.44	0.13	20.35	0.11	3.98	0.39	39.89	39.92
CaO	0.049	0.018	0.55	0.04	19.38	0.09			8.12	0.60	2.84	2.87
Na_2O			0.15	0.12	1.49	0.15			4.37	0.28	0.24	0.24
K_2O									1.27	0.19	0.02	0.01
P_2O_5	0.017	0.007	0.008	0.004	0.010	0.003					0.01	0.01
Mg#	90.3		90.7		91.0		77.2		68.7		90.4	90.3
n	10		10		10		8		4			
2-pyroxene temperature: 1030°C [17] or 1100°C [18]												

84-402	ol	±	opx	±	cpx	±	sp	±	Bulk rock	
Mode %[c]	71.6		23.7		3.6		1.1		measured	calculated
SiO_2	40.68	0.14	55.52	0.31	53.29	0.16			44.12	44.20
TiO_2			0.10	0.01	0.29	0.01	0.38	0.01	0.05	0.04
Al_2O_3	0.02	0.01	2.55	0.06	3.82	0.08	31.39	0.22	1.27	1.10
Cr_2O_3	0.03	0.01	0.67	0.03	1.53	0.02	36.16	0.33	0.46	0.63
FeO	8.87	0.08	5.57	0.04	2.49	0.03	14.20	0.26	7.86	7.92
MnO	0.14	0.01	0.14	0.01	0.08	0.01	0.13	0.03	0.12	0.14
NiO	0.38	0.01	0.10	0.01	0.05	0.01	0.19	0.03	0.31	0.30
MgO	49.76	0.26	33.61	0.16	16.69	0.15	17.36	0.13	44.54	44.39
CaO	0.06		0.79	0.04	20.45	0.17			0.87	0.97
Na_2O			0.09	0.01	1.18	0.09			0.07	0.06
P_2O_5	0.020	0.008	0.006	0.005	0.008	0.004			0.00	0.01
Mg#	90.9		91.5		92.3		68.6		91.0	90.9
n	10		10		7		10			
2-pyroxene temperature: 1010°C [17] or 1050°C [18]										

[a] Values represent 1σ standard deviation of multiple analyses, where n = number of analyses.
[b] Glass is an amphibole breakdown glass; the analysis reported here is the average of 4 different patches, where each patch is homogeneous and the differences between patches can be as much as 10 wt% for all elements, except K_2O which can differ by up to 15 wt% between different breakdown patches (see Appendix A).
[c] Modal mineralogies are calculated by least-squares mixing from whole-rock and mineral major-element compositions, except for glass, which was determined by least-squares mixing of trace elements. Oxides are given in wt%, Mg# = atomic ratio of $100 * Mg/(Mg + Fe)$.

threshold in trace-element studies on peridotites as a result of analytical advances in inductively coupled plasma mass spectrometry (ICP–MS), which is capable of rapid and precise, multi-element analyses spanning large concentration ranges and achieving low detection limits.

We present trace-element concentrations for bulk rocks and minerals in two peridotite xenoliths from southeastern Australia. The samples were chosen as representatives of fertile lherzolite and depleted harzburgite respectively. The distribution of 27 incompatible elements between the coexisting minerals, coupled with the bulk-rock data, allow us to make quantitative mass-balance calculations and evaluate the significance of grain boundaries and fluid inclusions in the incompatible-element budget of the upper mantle. Our data also bear on the debate regarding the mineralogical host of high-field-strength elements (HFSE) in the upper mantle (i.e., [10–12]).

2. Samples

The two peridotite xenoliths come from basanitic lavas from SE Australia and have been the subject of previous geochemical and isotopic investigations [13–15]. These samples have been chosen to represent and encompass the compositional spectrum seen in peridotite xenoliths [16]. One is a fertile lherzolite (2905), which has lost only a small amount of melt (i.e., it has 3.1% Al_2O_3 and 2.8% CaO) and retains a light rare-earth element (LREE) depletion, whereas the other is a refractory harzburgite (84-402) with a depleted major-element composition (1.3% Al_2O_3 and 0.9% CaO) that reflects the loss of a large amount of basaltic melt. Like most refractory harzburgites, this sample is LREE-enriched, indicative of metasomatic overprinting of the original depleted REE pattern [3]. Extensive electron probe analyses carried out in both thin sections and mineral mounts have established the compositional homogeneity of the minerals in these peridotites on both inter- and intra-grain scales (Table 1). In addition, previous isotopic investigations [15] document isotopic equilibration or near-equilibration between orthopyroxene, clinopyroxene and whole rock for the Rb–Sr and Sm–Nd systems. The lherzolite, from Mount Noorat, Victoria, has a granular texture with a well-developed foliation defined by spinels in thin section, and is comprised of olivine, orthopyroxene, clinopyroxene, spinel and rare amphibole breakdown products, which are described in detail below ([13]; modal mineralogy is given in Table 1). The harzburgite, from Mount Porndon, Victoria, has a protogranular texture composed of olivine, orthopyroxene, clinopyroxene, and spinel. No amphibole has been observed in this sample, although thin selvages of glass, fluid inclusions and tiny crystallites occur on some grain boundaries and may be the dispersed remnants of amphibole breakdown products. Equilibration temperatures, calculated using two-pyroxene geothermometry, range between 1010° and 1100°C and are indistinguishable between the two samples (Table 1).

The amphibole breakdown products in the lherzolite occur as glass pockets (1–2 mm across) containing small (≤ 20 μm), euhedral olivine, clinopyroxene, and spinel daughter crystals (Fig. 1). Similar occurrences have been previously described by Dasch and Green [13] and are comparable to others in SE Australian peridotites reported by Frey and Green [3] and Yaxley et al. [19] and to those described in xenoliths from the Eifel, Germany, by Stosch and Seck [20] and Yemen by Chazot et al. [21]. In some of these other cases relict amphibole remains within the center of the glass patches.

The glasses are enriched in Al_2O_3, SiO_2 and alkalis (Table 1) and have compositional affinities to olivine-hosted melt inclusions found in peridotite xenoliths worldwide [22]. Limited but distinct compositional differences occur from patch to patch (see footnote to Table 1 and Appendix A) and reflect variable extent of subsequent/concurrent reaction of the silicate melt with the surrounding mineral phases, as has been described elsewhere [19,20]. The occurrence of large vesicles within the glass patches attest to the exsolution of a vapor phase and accompanying expulsion of glass and vapor along grain boundaries. The primary amphibole composition can be reconstructed from the measured glass plus secondary phases compositions (see Appendix A). To do this we have employed the reaction stoichiometry that has been determined independently by both Chazot et al. and Yaxley et al. for the incongruent amphibole melting reaction in xenoliths from SE Australia and Yemen, i.e. (1.00) pargasitic amphibole ⇌

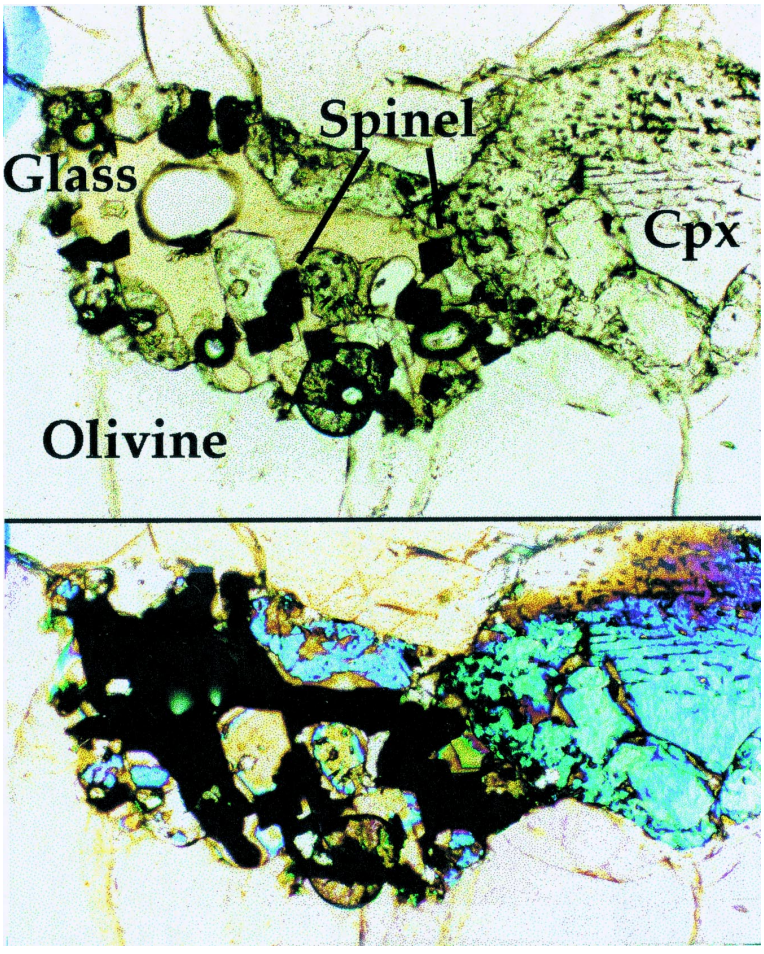

Fig. 1. Photomicrograph of amphibole breakdown products seen in peridotite sample 2905 under plane-polarized light (*upper*) and crossed nicols (*lower*). The field of view is ~250 μm. The glass is compositionally homogeneous in the melt pocket, but can vary in its composition by up to ~10% for most elements and up to 15% in the alkali metals between different melt pockets.

Table 2
ICP–MS operating conditions

	Solution nebulisation	Laser ablation
Forward (reflected) power (watt)	1350 (< 2)	1200 (< 2)
Gas flows (l/min)		
cool	14 (Ar)	14 (Ar)
auxiliary	0.7 (Ar)	0.7 (Ar)
carrier	0.9 (Ar)	0.3 (He) and 0.9 (Ar)
Detector mode	pulse counting	pulse counting
Sweep mode	peak hopping	peak hopping
Settle time (ms)	5	5
Dwell time (ms)	2.56–41	25–40
Points per peak	3	1
Analysis intervals	4 × 60 s replicates	60 s (peak), 120 s (background)

(0.40) glass + (0.35) clinopyroxene + (0.2) olivine + (0.05) spinel ± vapor.

3. Analytical techniques

Bulk-rock compositions were determined by X-ray fluorescence and ICP–MS (Tables 1–4) for major and trace elements, respectively. The major-element compositions of minerals were determined by electron microprobe [23] using a 25 keV accelerating voltage and a 40 nA beam current, which yields a focused beam that is 5 μm wide. The glass was analyzed using a beam current of 5 nA, accelerating voltage of 15 keV, and a defocused beam in order to minimize Na volatilization.

Table 3
Compositions of peridotite minerals determined by solution nebulization and laser ICP–MS

2905 Element	Laser[a] sp	Soln. sp	[a] Laser ol (2, 4)[b]	Soln. ol	Laser opx (3,[b]4)	Soln. opx	Laser cpx (2)	Soln. cpx	Laser glass [a]
Concentrations in ppm (μg/g):									
Li	1.01	0.72	1.40	1.70	0.96	1.05	1.25	1.31	
Sc	< 0.15	2.1	3.5 ± 0.1[c]	3.9	14.0 ± 0.1	60.2 ± 0.7	64.0	31.2	
Ti	720	720	24.0 ± 0.4	23.6	595 ± 8	568	2787 ± 40	2704	13,217
V	381	346	2.6	3.0	74	75	251	244	175
Ga	66.2	46.0	0.06	0.035	2.70	2.24	3.62	2.97	
Concentrations in ppb (ng/g):									
Rb	163	328	57	23	47	5.2	83	7.6	20,600
Sr	< 2		< 1	25.4	120 ± 17	129	61,000 ± 200	57,900	226,000
Y	< 1	200	39 ± 1	45	948 ± 5	1,071	18,400 ± 100	21,100	21,200
Zr	34	716	19.6 ± 0.3	118	1,460 ± 20	1,596	30,100 ± 300	33,400	53,800
Nb	< 3	85	1.0 ± 0.2	1.8	9.9 ± 0.4	6.4	214 ± 1	229	24,700
Cs		1.1		0.7		0.1		0.5	310
Ba	< 0.5	312	< 0.25	112.2	1.1--69.2	59	56.4 ± 1.7	182	371,000
La	< 0.4	11.9	< 0.2	1.4	1.3 ± 0.2	1.4	762	774	3,340
Ce	< 0.15	32.7	< 0.1	4.7	7.4 ± 0.3	10.1	2,840 ± 3	2,920	8,660
Nd	< 0.6	16.6	< 0.35	1.7	17.3 ± 0.2	19.8	3,680 ± 22	3,690	6,690
Sm	< 0.7	11.0	< 0.4		14.7 ± 0.2	19.0	1,540 ± 2	1,610	2,110
Eu	< 0.3	4.1	< 0.15	0.2	7.5 ± 0.4	9.1	642 ± 2	654	900
Cd	< 0.6	15.7	1.0 ± 0.5	1.4	48 ± 1	41.8	2,450 ± 4	2,520	2,830
Dy	< 0.35	32.5	3.1 ± 0.2	2.6	111 ± 1	116	3,135 ± 1	3,280	3,360
Er	< 0.4	23.9	6.8 ± 0.3	6.5	129 ± 2	137	2,016 ± 2	2,140	2,050
Yb	< 0.4	14.6	18.2 ± 0.7	17.6	208 ± 2	215	1,820 ± 15	1900	1,950
Lu		2.0		5.1		40.8		280	
Hf	< 0.3	19.6	0.3	2.6	43.8 ± 0.2	45.0	988 ± 1	1,020	1,240
Ta	0.4	58.3	< 0.05	6.5	0.7 ± 0.2	0.7	34.9 ± 0.2	41.0	1,190
Pb	< 2.0		< 1.1		2.7--45.2		50.5 ± 7.0		370
Th	< 0.1	5.0	< 0.03	0.8	0.16 ± 0.08	0.2	28.8 ± 3.3	30.7	231
U	< 0.1	1.3	< 0.03	0.4	0.18 ± 0.07	1.0	9.8 ± 0.9	10.4	77

Laser data for olivine and spinel determined at 50 Hz pulse repitition rate, remaining data collected at 10 Hz.

[a]Glass is an amphibole breakdown glass; the value reported here is the average of analyses of 4 different patches, where each patch is homogeneous and the differences between the patches can be as much as 10% relative for the major elements, except K_2O which is nearer 20%. Multiple analyses also demonstrate the trace elements to be homogeneous within the individual glass patches but significantly different between patches, particularly for the most highly incompatible elements (see Appendix A). Zr and Nb values for spinel (*italics*) are semi-quantitative only, as CrAr interference corrections are large (see text).

[b]Bracketed value is the number of LA–ICP–MS determinations performed, with the second number, where present, giving number of determinations for Ti, Zr, Nb, Ce, Yb, Hf and Ta.

[c]Quoted ± uncertainties are 1 standard deviation of multiple determinations. Note that a range of values is given in instances where repeat analyses gave disparate values (e.g., Ba in orthopyroxene).

Table 4
Compositions of peridotite minerals determined by solution nebulization and LA–ICP–MS

84-402 Element	Laser sp	Soln. sp	Laser ol (2, 3)[b]	Soln. ol	Laser opx (1, 2)	Soln. opx	Laser cpx (2)	Soln. cpx	NIST glass 612 [a]	Signal intensity (counts/sec/ppm)
Concentrations in ppm (μg/g):										
Li	0.38	0.202	1.42 ± 0.05[c]	1.48	1.5	1.35	1.0 ± 0.2	1.95	40.4	8,750
Sc	1.4	2.9	4.9 ± 0.3	3.7	19.7	20.8	89.9 ± 0.2	94.4	39.0	27,000
Ti	1607	1607	24.3 ± 0.9	27.4	615 ± 3	531	1572 ± 50	1512	40.0	1,600
V	653	567	2.99 ± 0.02	2.8	76.6	69	231 ± 4	219	38.0	19,000
Ga	33.4	25.2	0.081 ± 0.014	0.048	2.22	1.74	2.45 ± 0.02	2.01	36.0	13,000
Concentrations in ppb (ng/g):										
Rb	168	680	108 ± 9	47	59	71	70 ± 2	34	31,400	32,000
Sr	7		< 2	331	335	370	167,000 ± 1000	155,000	78,000	59,000
V	1.4	22	29 ± 1	37	771	775	11,000 ± 100	12,300	40,500	48,000
Zr	*194*	452	52 ± 3	244	2,540 ± 100	2,490	46,300 ± 1,200	50,400	38,300	23,000
Nb	*110*	140	9.5 ± 1.6	45	78 ± 1	72	1,490 ± 180	1460	39,700	42,000
Cs		0.9		2.0		0.5		0.4		
Ba	< 1.4	80	< 0.56	214	1.4	78	110–3610	211	38,500	64,000
La	< 0.9	6.2	< 0.35	20.2	11.0	14.8	5,870 ± 30	5780	35,500	69,500
Ce	< 0.7	14.2	< 0.24	40.6	48.6 ± 2.5	48.4	13,280 ± 80	13370	38,000	79,500
Nd	< 2.4	8.1	1.2 ± 0.4	17.5	62.7	62.4	10,250 ± 190	10140	35,200	16,400
Sm	< 1.9	5.4	< 0.68	3.2	36.2	35.7	2.780 ± 60	2830	36,800	26,000
Eu	< 1.0	12.1	< 0.34	1.8	15.1	16.1	991 ± 11	960	35,000	49,000
Gd	< 2.3	4.5	1.0 ± 0.2	4.2	69.7	59.1	2,740 ± 40	2850	37,500	19,000
Dy	< 1.8	6.2	2.4 ± 0.14	5.0	109	95.9	2,260 ± 30	2280	36,000	22,000
Er	< 1.4		4.1 ± 0.4	5.5	94.9	87.6	1,096 ± 11	1112	38,600	28,000
Yb	< 1.6	3.2	11.4 ± 0.5	11.7	143 ± 1	128	881 ± 10	893	39,100	28,000
Lu		0.3		2.7		23.1		131		
Hf	4.6	16.6	0.6 ± 0.2	5.1	67 ± 2	60.7	1337 ± 27	1320	37,700	22,000
Ta	12.2	26.3	0.21 ± 0.09	14.1	4.7 ± 0.1	6.6	216 ± 11	215	40,100	69,000
Pb	< 3.4		< 1.4		2.8		202 ± 20		38,600	38,000
Th	< 0.52	2.6	< 0.19	4.9	4.3	6.6	608 ± 11	620	37,800	60,000
U	< 0.43	0.9	< 0.15	0.7	3.0	3.3	135 ± 6	136	37,400	81,000

All laser data collected at 10 Hz, except cpx (5 Hz).

[a] NIST glass 612 values reported here are those adopted as the laser reference standard, and the signal intensities refer to the average intensities per ppm obtained for the NIST 612 glass, ablating at 10 Hz with a 200 μm spot. Zr and Nb values for spinel (*italics*) are semi-quantitative only, as CrAr intereference corrections are large (see text).

[b] Bracketed value is the number of LA–ICP–MS determinations performed, with the second number, where present, giving number of determinations for Ti, Zr, Nb, Ce, Yb, Hf and Ta.

[c] Quoted ± uncertainties are 1 standard deviation of multiple determinations. Note that a range of values is given in instances where repeat analyses gave disparate values (e.g., Ba in orthopyroxene).

Mineral and glass trace-element compositions were determined by ICP–MS solution chemistry and laser ablation (LA) methods [24–26]. Operating conditions employed for the Fisons PQ2 STE ICP–MS instrument at the Research School of Earth Sciences, ANU, are listed in Table 2.

For solution analyses, aliquots of minerals were hand-picked to optical purity then leached in an ultrasonic bath using the following protocol: 3 *N* HCl for 30 min, 5% HF for 20 min and 3 *N* HCl for 30 min, followed by distilled water for 30 min. The purified and leached mineral separates (20–40 mg aliquots) and 100 mg aliquots of the bulk-rock powder were dissolved in a mixture of ultrapure, concentrated HF–HNO_3 and then spiked with a mixed multi-element/isotope internal standard solution prior to analysis [24]. Complete dissolution of spinel was achieved by first powdering the purified separates in an agate mortar and pestle, then completely dissolving this powder in screw-top Teflon beakers (as described above), by alternating between the hot-plate and an ultrasonic bath over a period of ~ 7 days. Polished grain mounts for each sample, and a polished thin section (for the glass analyses) were analyzed by LA–ICP–MS.

The LA–ICP–MS system at ANU incorporates an ArF (193 nm, 20 ns pulse width) EXCIMER laser and custom built sample cell and transport system. The details of this system are described in a separate publication [25], and here we only present information pertinent to the present experiment. The EXCIMER laser illuminates a mask that is imaged at $20\times$ demagnification on to the sample surface with an aplanatic doublet lens of 150 mm focal length. This imaging arrangement produces a top-hat beam profile that results in sharp-edged ablation holes of set dimensions (from <20 μm to >200 μm), that are changed by varying the size of the mask. Thus changing spots size is independent of the energy density delivered to the sample surface, thereby maintaining constant ablation conditions. Typical laser output energy of 100 mJ/pulse in a beam of approximately 20×8 mm, results in a measured energy density on the sample of the order of 10 J/cm^2, after passage through the mask and beam delivery optics.

In this study, laser sampling was performed in a He atmosphere using a 200 μm spot size for minerals, and a 50 μm spot size for glasses. Uniform ablation of 0.1 μm/pulse is achieved across the ablation site [26] with the specified energy density. At the routine laser pulse repetition rates used in this study of 5 and 10 Hz the ablation rate is ~ 0.5 and ~ 1.0 μm/s, respectively. The resulting pits have small aspect ratios (30 or 60 μm deep/200 μm wide) and are therefore not subject to adverse elemental fractionation [26]. In order to extend detection limits, the laser repetition rate was increased to 50 Hz for additional olivine and spinel analyses in sample 2905.

Data acquisition was performed by peak hopping (one point per isotope) in pulse counting mode, acquiring individual intensity data for each analyte isotope during each mass spectrometer sweep (~ 1 s). A total of 120 sweeps (120 s), comprising a gas background interval of 60 sweeps followed by an ablation interval of 60 sweeps were performed for each analysis. Signal intensities for the high-mass elements were typically in the range 15 000–80 000 counts s^{-1} ppm^{-1} (Table 4), and vary as a function of isotope abundance, differential ionization of the elements in the ICP, and increased sensitivity at higher masses. The sensitivities for the high-mass analytes equate to a laser sampling and ICP–MS transmission efficiency of the order of ~ 1 ion detected per 10 000 ablated.

Data reduction followed a protocol essentially identical to that outlined by Longerich et al. [27], except for the estimation of single acquisition detection limits, which were calculated from the variance of the mean background count rate obtained by integrating the background intervals from each analysis and the ensuing analysis (120 sweeps total background). Limits of detection are typically in the range 0.2–2 ppb for most high-mass elements (>80 amu), and between 1 and 100 ppb for lower-mass elements. With increased laser repetition rates (up to 50 Hz), detection limits have been reduced to as low as 30 ppt for some elements (see Table 3).

Analyte concentrations were determined using the mean background intensities of each isotope and ratioing these corrected intensities to that of the internal standard isotope for each mass spectrometer sweep. A total of ~ 60 replicate measurements was thereby acquired for each analyte isotope in each analysis, with the internal standard correcting for

variation in instrument and ablation yield. An instrumental drift correction (external standardization) was also applied by applying a linear correction to measured analyte intensities between repeat measurements of the NIST 612 glass. ^{43}Ca has been routinely employed as the internal standard, based on electron microprobe measurements of CaO contents in the minerals and glasses. The only exception occurs in the case of spinel, for which we employed ^{49}Ti as the internal standard based on Ti concentrations measured by solution nebulization ICP–MS.

The LA–ICP–MS spectra were obtained with unit mass resolution. They require few if any interference corrections, due to very low molecular and doubly charged species production. In this study ThO^+/Th^+ was maintained below 0.5% and Ba^{2+}/Ba^+ below ~0.1%, both limits being an order of magnitude lower than encountered during solution–ICP–MS analysis. However, the high sensitivity of our instrument makes interferences from less familiar molecular species such as nitrides and argides important in some instances. The most significant in this case is the analysis of Nb and Zr in spinels, which is prone to CrAr interferences. However, by monitoring the nominal analyte intensities of ^{90}Zr (I_{90}) and ^{92}Zr (I_{92}), the production of $^{52}Cr^{40}Ar$ could be estimated as $^{52}Cr^{40}Ar = (I_{92} - AI_{90})/(1 - AB)$, where A and B are the instrumental mass bias-corrected isotope abundance ratios for $^{92}Zr/^{90}Zr$ and $^{52}Cr/^{50}Cr$, respectively), thereby enabling the $^{53}Cr^{40}Ar$ contributions to ^{93}Nb and $^{50}Cr^{40}Ar$ to ^{90}Zr to be calculated and stripped accordingly. Because the corrections are

Table 5
Composition of bulk peridotites

Element	2905 bulk rock	Laser calculated	Solution calculated	84-402 bulk rock	Laser calculated	Solution calculated
Li	1.35	1.25	1.47	1.12	1.41	1.45
Sc	14.2	13.6	14.9	10.1	12.1	10.6
Ti	619	671	613	251	280	218
V	67.6	61.7	60.8	37.7	41	32
Ga	2.26	2.60	1.84	1.18	1.25	0.79
Rb	0.234	0.20	0.146	0.069	0.066	0.074
Sr	8.51	10.04	9.32	5.56	6.48	5.84
Y	3.22	3.05	3.30	0.68	0.65	0.61
Zr	5.33	4.92	5.36	2.77	2.47	2.45
Nb	0.178	0.192	0.183	0.219	0.221	0.245
Ba	1.87	2.39	2.34	0.506	0.584	0.628
La	0.170	0.129	0.127	0.262	0.228	0.226
Cc	0.536	0.461	0.456	0.577	0.518	0.504
Nd	0.556	0.578	0.551	0.403	0.400	0.367
Sm	0.218	0.241	0.237	0.114	0.113	0.104
Eu	0.094	0.101	0.097	0.040	0.041	0.037
Gd	0.363	0.383	0.372	0.124	0.121	0.111
Dy	0.477	0.499	0.499	0.115	0.116	0.101
Er	0.335	0.335	0.342	0.0687	0.0700	0.0611
Yb	0.325	0.332	0.334	0.0730	0.0810	0.0681
Lu	0.052		0.051	0.0122		0.0115
Hf	0.155	0.156	0.160	0.0700	0.0682	0.0618
Ta	0.0128	0.0126	0.0179	0.0129[a]	0.0151	0.0253
Pb	0.092	0.010	0.785	2.120	0.009	1.1617
Th	0.0120	0.0055	0.0062	0.0320	0.0264	0.0295
U	0.0041	0.0019	0.0024	0.0100	0.0064	0.0066

[a] Value is estimated from Nb (assuming Nb/Ta = 17), due to Ta contamination of the rock powder by the milling process.
Element abundances are given in ppm (μg/g). Mineral proportions used in the calculated composition are given in Table 1, except for the addition of 1.6% of the calculated amphibole composition (see Appendix A) in the case of the 2905 laser estimate, and 0.2% amphibole in the 84-402 laser estimate, based on the 84-402 clinopyroxene composition and the 2905 amph/cpx distribution coefficient (see text and caption to Fig. 7).

large, up to 85%, the resulting Nb and Zr analyses have considerable uncertainties and are provided for information only (Tables 3 and 4). A possible contribution from $^{29}Si^{14}N$ to the intensity of the internal standard isotope ^{43}Ca was found to be negligible based on no additional ^{43}Ca signal being observable during ablation of semiconductor grade Si metal, despite yielding intensities of several million counts per second on ^{29}Si.

4. Results

Our mineral, glass, and whole-rock analyses are reported in Tables 1, 3–5 and plotted in Figs. 2–4. The repeatability of duplicate and triplicate LA–ICP–MS analyses is generally excellent, as is agreement between laser ablation and solution ICP–MS data for orthopyroxene and clinopyroxene, ranging over 8 orders of magnitude (Fig. 2). These data

Table 6
Mean compositions of individual glass patches in lherzolite 2905, as determined from duplicate EMP and LA–ICP–MS analyses, and reconstructed amphibole composition, based on the average glass composition, cpx/melt partition coefficients from Chazot et al. [21] and microprobe analyses of clinopyroxene, olivine and spinel in glass patches

	Glass patch #1	Glass patch #2	Glass patch #3	Glass patch #4	Mean glass	$D^{cpx/melt}$ (Chazot)	Calc. amph
(wt%):							
SiO_2	57.06	54.63	56.11	54.32	55.53		47.50
TiO_2	2.00	2.30	2.28	2.58	2.29		1.27
Al_2O_3	21.31	21.48	21.00	21.20	21.25		14.41
FeO	3.10	3.23	3.13	3.46	3.23		2.72
MgO	3.49	4.29	3.84	4.30	3.98		18.63
CaO	7.36	8.70	7.92	8.49	8.12		9.94
Na_2O	4.62	3.96	4.40	4.48	4.37		2.04
K_2O	1.06	1.42	1.43	1.15	1.27		0.49
(ppm):							
Sc	29.2	33.0		31.4	31.2		
Ti	10950	13250	14580	14090	13220	0.452	7380
V	155	214		158	175		
Rb	14.3	21.4	32.5	14.4	20.6	0.071	8.77
Sr	162	316	231	197	226	0.128	100.7
Y	18.3	23.3	21.2	22.05	21.2	1.132	16.89
Zr	36.22	72.52	53.2	53.4	53.8	0.242	26.09
Nb	17.65	28.0	25.1	27.8	24.7	0.013	9.97
Cs	0.109	0.258	0.730	0.141	0.309	0.000	0.124
Ba	263	367	550	304	371.2	0.001	148.5
La	1.30	5.64	3.37	3.04	3.34	0.137	1.495
Ce	4.50	13.17	8.54	8.42	8.66	0.265	4.26
Nd	4.63	8.82	6.26	7.08	6.69	0.638	4.17
Sm	1.732	2.32	1.997	2.39	2.11	1.005	1.585
Eu	0.729	1.057	0.886	0.948	0.905	1.028	0.688
Gd	2.39	3.16	2.65	3.11	2.83	0.987	2.11
Dy	2.86	3.54	3.28	3.77	3.36	0.957	2.47
Er	1.81	2.23	1.88	2.30	2.05	0.863	1.442
Yb	1.69	2.09	1.93	2.09	1.948	0.870	1.373
Hf	0.907	1.539	1.104	1.397	1.237	0.230	0.594
Ta	0.830	1.325	1.156	1.441	1.188	0.015	0.475
Pb	0.315	0.260	0.591	0.318	0.371	0.000	0.148
Th	0.057	0.419	0.231	0.218	0.231	0.007	0.093
U	0.020	0.146	0.075	0.067	0.077	0.000	0.031

illustrate the wide dynamic range, high sensitivity, matrix tolerance, and the accuracy of our laser technique in the absence of suitable standard reference materials for these minerals in the concentration ranges measured. On the other hand, agreement between laser and solution ICP–MS for olivine and spinel, while reasonable for the heavy rare-earth element (HREE) in olivine, is relatively poor for most other elements (Tables 3 and 4), for which consistently higher concentrations of incompatible trace elements are measured by the solution technique. This disparity arises from impurities in the minerals separated for solution analyses, despite our best efforts at obtaining ultra-clean mineral separates. The same problem is also responsible for the higher Ba values measured by the solution technique for both orthopyroxene and clinopyroxene (Fig. 2). We believe these results highlight the significant advantages of in situ laser sampling methods for avoiding problems associated with impurities in otherwise homogeneous mineral compositions. Nonetheless, we report comparatively high ^{85}Rb values and degraded repeatability of some Ba measurements by laser ablation. In the case of Rb, these results reflect scavenging of Rb from the sample cell during ablation, a problem that has subsequently been overcome by modifications to the sample cell design.

Fig. 3 illustrates the relative distribution of REE between minerals in both peridotites. Clinopyroxene and the amphibole breakdown glass contain the greatest REE concentrations and thus define the pattern of the bulk rock. Orthopyroxene and olivine are LREE depleted with concentrations 2 to >4 orders of magnitude lower than clinopyroxene and amphibole. These results are comparable to those found in earlier studies on spinel peridotites [3,29]. REE data for chrome spinels are not shown on this diagram as laser ablation measurements reveal that the concentrations are below detection limits (sub-ppb levels). The higher concentrations of REE reported for the solution chemistry analyses of spinels are considered to be compromised by the presence of trace silicate impurities in the opaque spinel separates.

Relative concentrations of non-rare-earth, incompatible elements are shown in Fig. 4. As with the REE, clinopyroxene and amphibole breakdown glass have the highest concentrations of most of these elements and olivine the lowest, with orthopyroxene falling in between. However, Li is distributed sub-

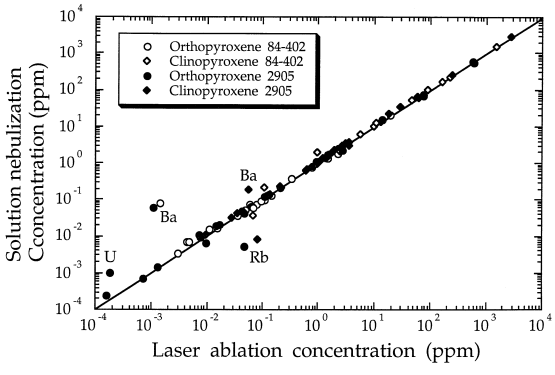

Fig. 2. Comparison of trace-element abundances in clinopyroxene and orthopyroxene from 2905 as determined by solution nebulization ICP–MS and laser ablation ICP–MS. Element abundances are given in ppm (μg/g). Anomalies in Ba and U are likely due to impurities in the mineral separates, whereas the anomalies in Rb are due to high background during laser ablation analyses (see text).

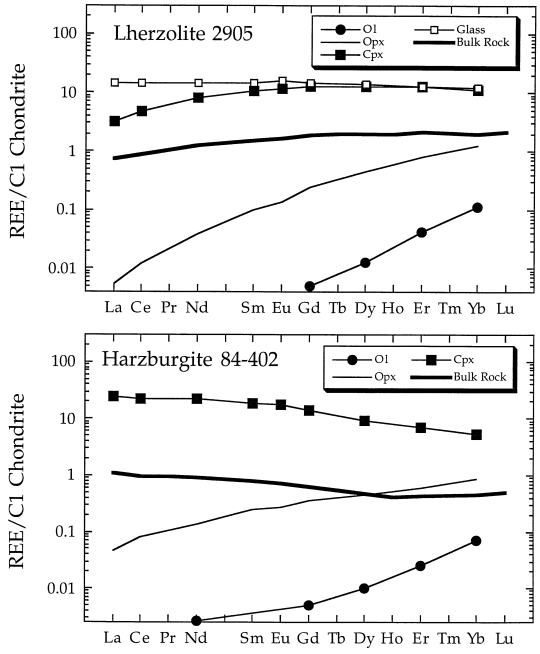

Fig. 3. REE diagram for bulk-rock peridotites and their minerals for sample 2905, a LREE-depleted, fertile lherzolite and 84-402 and a LREE-enriched, harzburgite. REE abundances are normalized to C1 chondrites using the values reported in McDonough and Sun [28]. REE abundances in the spinels are at or below detection limits. *Ol* = olivine; *Opx* = orthopyroxene; *Cpx* = clinopyroxene; *Amph* = amphibole breakdown glass.

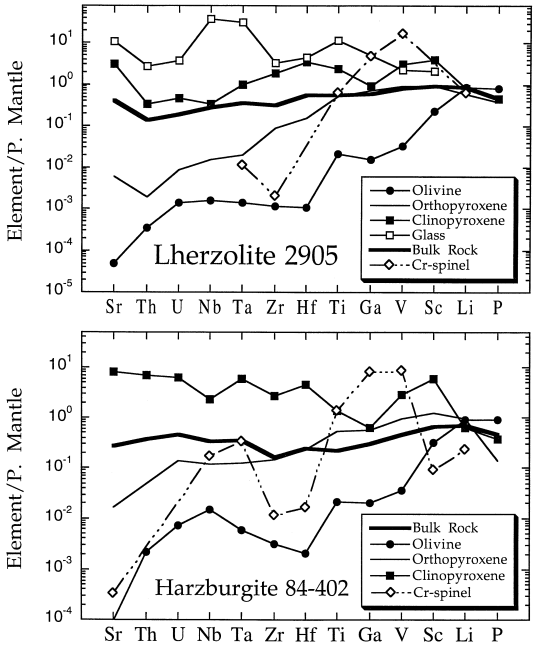

Fig. 4. Mantle-normalized diagram for the non-rare-earth incompatible elements in bulk-rock peridotites and their minerals. *Upper*: sample 2905, a LREE-depleted, fertile lherzolite. *Lower*: 84-402, a LREE-enriched, harzburgite. The elements are arranged in order of increasing incompatibility during mantle melting from right to left, as defined from studies of MORB and OIB (exceptions are Sr and P, which would normally be plotted between Ta and Zr). Element abundances are normalized to the primitive mantle values of McDonough and Sun [28]. *Ol* = olivine; *Opx* = orthopyroxene; *Cpx* = clinopyroxene; *Glass* = amphibole breakdown glass; *Sp* = spinel.

equally amongst the peridotite minerals since it substitutes for Mg (due to their similar ionic radii of 0.80 and 0.82 Å). Spinels (both Al-rich in the lherzolite and Cr-rich spinels in the harzburgite) are important hosts of Ga, V and Ti, but are depleted in most of the other elements. Although the Cr-rich spinel in the harzburgite has Nb and Ta contents greater than those of orthopyroxene and olivine, its low modal abundance does not make it an important host of these elements in the mass balance (see Fig. 8). There is a general tendency for the elements on the left-hand side of Fig. 4 (greater incompatibility) to be more concentrated in the clinopyroxenes and amphibole breakdown glass. It is also interesting to note that the low Nb/Ta and Zr/Hf ratios in clinopyroxene in the lherzolite (6 and 30, respectively) are complemented by high Nb/Ta and Zr/Hf ratios in the glass (20 and 43, respectively) giving the bulk-rock Nb/Ta of 14 and Zr/Hf of 34 — similar to the chondritic values (17 and 37, respectively [30]).

5. Mass balance

Table 5 compares measured bulk-rock peridotite compositions with those calculated from the mineral phases as determined by both solution and laser ICP–MS. Many of the highly incompatible trace elements show significant deficiencies in the lherzolite if the data for the amphibole breakdown products are excluded. These deficiencies amount to more than 60% of the whole-rock budgets of Ba, Nb, Ta, Th and U, and smaller but still significant shortfalls for the LREE and Sr (Fig. 5). Most moderately incompatible trace elements balance to within 5% of the measured bulk peridotite element concentrations.

Inclusion of amphibole breakdown products in the mass balance for the lherzolite requires an accurate estimate of their modal abundance. The occurrence of several individual amphibole breakdown patches with dimensions on the order of 1–2 mm, in 3 separate thin sections, suggests a modal abundance of ~1 vol%. An estimated amphibole modal abundance of ~1.6 wt% is derived by minimizing of the residual sum of squares of the trace-element mass balance. This amount of amphibole produces an excellent mass balance for all the incompatible elements except for Th, U which remain under budgeted by ~50% (Fig. 5). We believe this is an acceptable outcome given the low concentrations of these elements in the bulk rock (i.e., 4.1 ppb U and 12 ppb Th).

A similar pattern of deficiencies observed in the element mass balance for the harzburgite leads us to believe that the glass and crystallites seen distributed on grain boundaries have bulk compositions similar to the amphibole breakdown patches observed in the lherzolite. Using partition coefficients between the amphibole breakdown products and clinopyroxene in the lherzolite, we are able to calculate a provisional amphibole composition for the harzburgite based on its clinopyroxene composition (see Appendix A). From this we obtain a good mass balance for the harzburgite with only 0.2 wt% of the amphibole component (Fig. 5), consistent with the small volume of the grain boundary impurities in this sample.

Fig. 6 illustrates the fractional contribution of each mineral to the bulk-rock elemental inventory. Clinopyroxene is the dominant host for most incompatible trace elements in the spinel peridotite facies of the upper mantle. When present, however, amphibole is the most important host for Ba, Nb and Ta

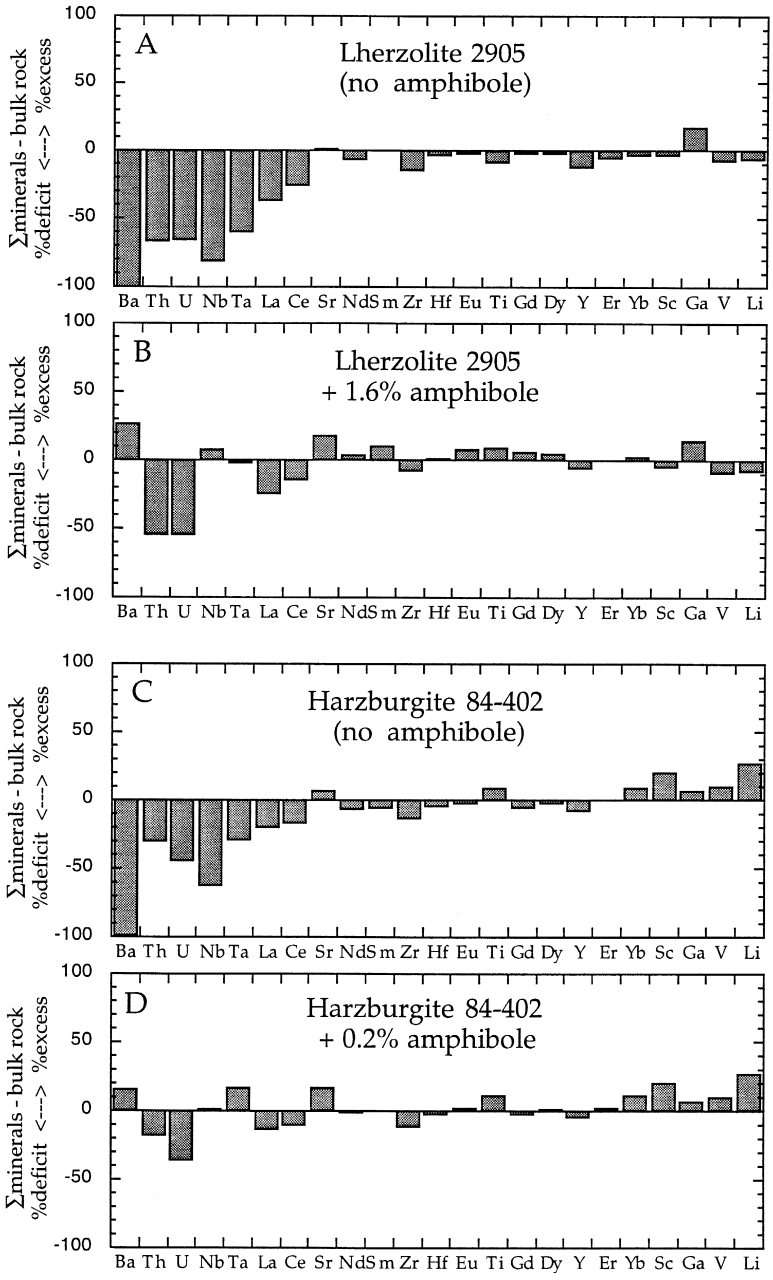

Fig. 5. Mass-balance results for the harzburgite (84-402) and lherzolite (2905), showing the net shortfall or surplus of each element calculated from the sum of the constituent minerals as compared to their measured bulk rock abundances. Panel (D) illustrates the improved mass-balance result for 84-402 by adding 0.2 wt% of an appropriate amphibole composition estimated for this sample, based on the 84-402 clinopyroxene composition and amphibole/clinopyroxene distribution coefficients determined from sample 2905.

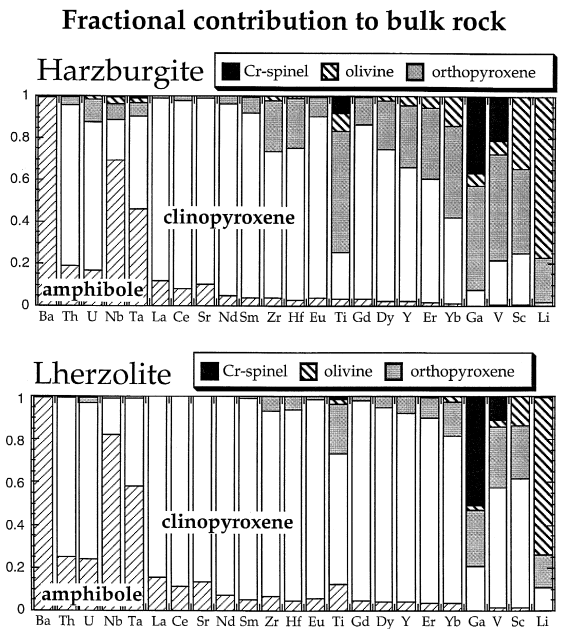

Fig. 6. Relative contributions of the individual mineral phases to the trace-element budgets for harzburgite 84-402 and lherzolite 2905. The result for sample 84-402 includes 0.2 wt% of a calculated equilibrium amphibole composition, as in panel (D) of Fig. 5. This figure illustrates the dominant role of clinopyroxene as host for the incompatible trace elements in the spinel peridotite facies of the upper mantle, as well as the significance of amphibole as a host for Ba, Nb and Ta. Orthopyroxene has an increasingly important role as a trace-element host as the peridotite composition becomes more refractory (cf. 84-402 vs. 2905), particularly for Ti and the more moderately incompatible elements.

(even at < 1 wt% amphibole). As the peridotite composition becomes more refractory (cf. 84-402 vs. 2905), orthopyroxene is increasingly important as a trace-element host, particularly for Ti and the more moderately incompatible elements (e.g., [10]). Spinel is only an important host for Ga and V, despite the fact that it can have Nb and Ti contents higher than those of orthopyroxene.

6. Discussion

6.1. The significance of amphibole

The amphibole breakdown products in lherzolite 2905 include the exsolution of a vapor phase. We suggest that vapor bubble nucleation and growth promotes hydraulic injection of the silicate melt and vapor along grain boundaries, and the development of fluid and melt inclusion trails through fractured mineral grains (as observed in harzburgite 84–402). These phenomena have been described by Yaxley et al. [19] for other SE Australian peridotites, who concluded that the glasses must have been produced in the xenoliths immediately before or shortly after entrainment of the xenoliths in their host basalts. Hence, grain boundaries containing materials enriched in incompatible trace elements [31] may not reflect the original distribution of these elements under upper-mantle conditions.

Given this observation, the data presented here demonstrate two simple but significant points: (1) amphibole (now present as glass patches and daughter crystals) plays an important role, even at sub-percent mode levels, in accounting for the budget of the highly incompatible elements in these peridotites, particularly Ba, Nb and Ta; and (2) the budgets of the incompatible trace elements can be accounted for by the solid mineral phases present at upper-mantle conditions, that is, within the crystal structures of olivine, spinel, clinopyroxene, orthopyroxene and amphibole. Grain boundaries, fluid inclusions and exotic accessory phases, such as rutile or ilmenite (e.g., 12) are not required repositories.

Our results call into question the general importance of minute Nb- and Ta-rich ilmenite and rutile crystals, which have been observed on spinel surfaces in some peridotite xenoliths by Bodinier et al. [12] and in our own studies of Tanzanian peridotite xenoliths (unpublished results). We have examined the samples investigated here, as well as other SE Australian peridotites by optical microscopy, backscattered electron imaging and electron microprobe spectrometry. There is no evidence rutile rims on spinels in these samples. Thus, although rutile is an important hosts for HFSE in some metasomatized xenoliths, it is not ubiquitous and does not account for the common Nb mass-balance problem observed in peridotites by ourselves and others [32].

Our results also preclude that olivine or orthopyroxene are significant repositories for Nb and Ta, or other highly incompatible trace elements (Th, U, Rb, and Ba and the LREE) in the upper mantle as suggested by Sun and Kerrich [33].

The compositions of the amphibole breakdown glasses observed here are similar to those observed in peridotite xenoliths worldwide [22].

These are rich in Si and Al and have major-element compositions [22]

> ... are more akin to continental than to oceanic crust.

However, the trace-element compositions of our glasses are unlike continental crust, being strongly enriched in Nb relative to La, which is the antithesis of the fractionation observed in continental crust [34] We conclude, in concurrence with Yaxley et al. [19], that breakdown of hydrous phases is a viable model for the origin of some xenolithic glasses and show below that trace-element determinations can be a diagnostic tool for evaluating the origin and significance of these glasses.

6.2. Subsolidus partitioning

The data reported here constitute one of the most comprehensive sets of mineral partitioning data for peridotites yet reported. As such, they offer new insights into subsolidus partitioning of trace elements under upper-mantle conditions. They also offer a means of evaluating the reliability of using subsolidus partition coefficients to infer crystal/liquid *D*-values, which is commonly done for minerals in which the latter are difficult to determine experimentally (e.g., $D^{opx/liq}$, $D^{ol/liq}$, $D^{sp/liq}$).

Fig. 7 shows that orthopyroxene–clinopyroxene and olivine–clinopyroxene partition coefficients are remarkably similar in both peridotites. Subtle, but significant differences in partition coefficients exist for Nb and Ti: in the harzburgite $D^{opx/cpx}$ and $D^{ol/cpx}$ are higher by a factor of 1.8 compared to the lherzolite. Spinel/clinopyroxene partition coefficients (not shown) are more variable, which may reflect crystal chemical controls on partitioning given the different spinel chemistries in the two samples (Tables 1, 3 and 4). ''Amphibole''/cpx partition coefficients are very high for Nb (46), Ta (14) and particularly Ba (up to 2600), whereas most other elements have partition coefficients < 10 and typically near 1 (Fig. 7). This pattern of element partitioning is similar to that of amphibole/cpx pairs measured by ion microprobe and by solution–ICP–MS for mantle peridotites from a variety of settings [11,21,35–38]. The close agreement between our data and these earlier results supports our, and others' contention that these glasses are amphibole breakdown products [3,19].

In order to use subsolidus partition coefficients to infer crystal–liquid partition coefficients one must establish how sensitive subsolidus partitioning is to changing *P*, *T*, bulk composition and metamorphic facies (which changes the compositions of coexisting minerals). Our remaining discussion will focus on orthopyroxene–clinopyroxene partitioning, as few comparative data are available for the other minerals.

For the two samples measured here, the phase assemblage is identical (i.e., ol, opx, cpx, sp and (minor) amph), *P* and *T* of equilibration are similar, but bulk compositions, and attendant mineral compositions, differ significantly. As shown above, the relative partitioning behavior of most incompatible elements (except Nb and Ti) appears to be identical between the two samples, implying that bulk compositional differences, and their attendant mineral compositional changes, play only a minor role in the subsolidus partitioning of these elements. However, in the more refractory peridotite, Ti is preferentially partitioned into the olivine and orthopyroxene over clinopyroxene (Fig. 7).

To evaluate the effects of the intensive variables on trace-element partitioning, we compare our results to data from the literature. Fig. 8 shows opx/cpx partition coefficients for a range of elements plotted against equilibration temperature. The LREE, as exemplified by Ce, show an large range in $D^{opx/cpx}$ (factor of 30), which correlates with reciprocal equilibration temperature. The HREE (e.g., Yb), show a narrower range of $D^{opx/cpx}$ (factor of 3), which also correlates with equilibration temperature. Partition coefficients for Sr (not shown) and Zr, a HFSE, vary by factors of 2–3 and also correlate with reciprocal temperature. The trends of the limited $D^{opx/cpx}$ data for garnet peridotites are unclear, and more data are needed before their significance can be evaluated. The correlations seen here likely reflect substitution of these elements on to the M2 site in pyroxenes [29,44], the same site in which Ca is sited.

In contrast to the above elements, $D^{opx/cpx}$ for Ti, Nb and V vary by up to an order of magnitude and do not appear to be a simple function of temperature

(Fig. 8). These elements have smaller radii (e.g., 0.6–0.64 Å for octahedral coordination, cf. > 0.7 Å for Zr and the REE) and may substitute into multiple sites in pyroxenes and/or (for V) be controlled by variations in oxygen fugacity. Interestingly, spinel-facies peridotites have $D^{opx/cpx}$ values for Nb and Ti

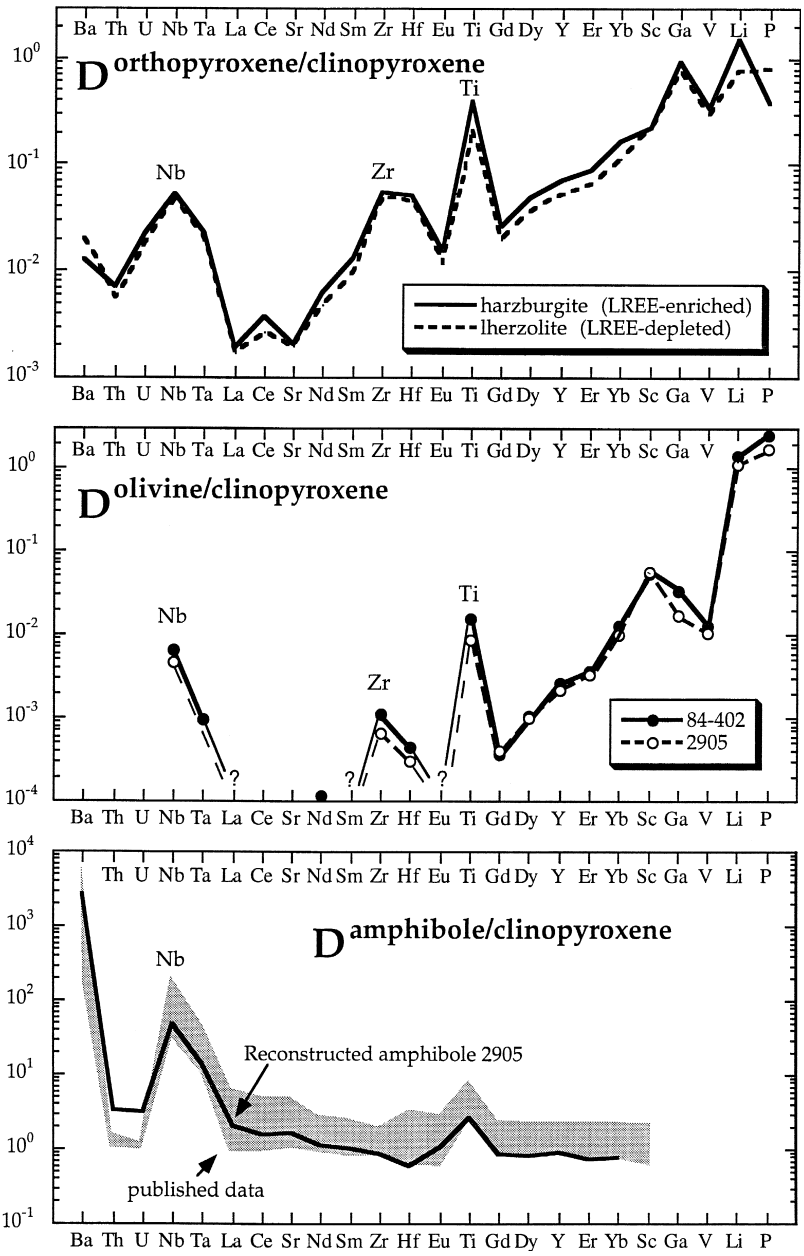

Fig. 7. Mineral/mineral partition coefficients for co-existing phases in the lherzolite (2905) and harzburgite (84-402). Many of the olivine data for the highly incompatible elements are at the level of detection limits. Bottom panel shows amphibole/clinopyroxene partitioning from this study (reconstructed amphibole from sample 2905, see Appendix A) compared to field of published results [11,21,35–38]. In addition to our study, Th and U partitioning data are only available from Chazot et al. [21] and Ionov and Hofmann [35]. *Ol* = olivine; *Opx* = orthopyroxene; *Cpx* = clinopyroxene; *Glass* = amphibole breakdown glass.

that are generally lower than those of garnet-facies peridotites. Although it will be necessary to verify these observations with additional data, they suggest that pressure, and the associated changes in crystal chemistry accompanying changing mineralogy/metamorphic facies, may also play a role in subsolidus partitioning of some trace elements.

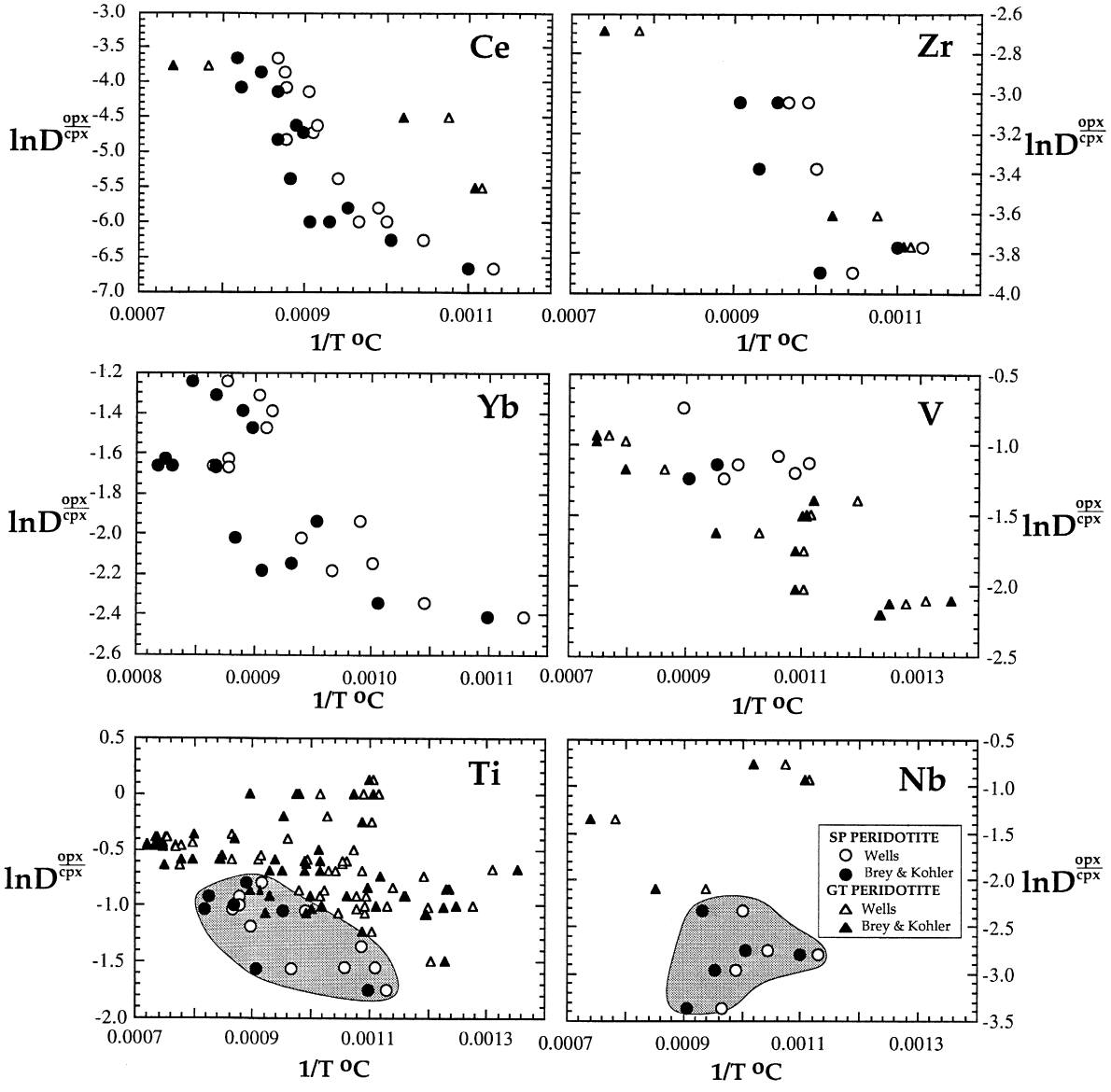

Fig. 8. $1/T$ (°C) vs. ln $D^{Opx/Cpx}$ for Ce, Yb, Ti, Zr, V and Nb in spinel- (*circles*) and garnet-facies peridotites (*triangles*). Temperatures are derived from two calibrations of the two-pyroxene thermometer [17,18], thus two points are plotted for each sample (in some cases the two temperatures coincide). REE partitioning data are from both bulk mineral [20,35,39] and in situ methods (this study and [40]). Ti data are either by electron microprobe studies in which attention was paid to obtaining high-quality analyses [10,41,42] or from LA–ICP–MS (this study). V data from electron microprobe [41,42] or LA–ICP–MS (this study). Zr and Nb data are from ion microprobe [40], solution ICP–MS [35,39] and LA–ICP–MS (this study). Data for peridotites with multiple generations of minerals were omitted (e.g., [11,43]).

The above observations show that changing T, and possibly P and phase assemblage exert controls on the subsolidus partitioning of incompatible trace elements in the upper mantle, as shown in earlier studies [11,45]. This does not bode well for the derivation of crystal–liquid partition coefficients from solid–solid D values. Moreover, this study highlights the need for further systematic, high-precision, trace-element determinations for minerals in natural peridotites and experimental charges in order to evaluate the relative effects of T, P, f_{O_2} and phase composition on subsolidus partitioning.

7. Conclusions

We have determined the concentrations of major elements and 27 trace elements in coexisting spinel, olivine, orthopyroxene and clinopyroxene from two spinel peridotite xenoliths from SE Australia: one a fertile lherzolite, the second a refractory harzburgite. From these data we draw the following conclusions:

(1) In situ laser ablation analyses compare well with analyses made on dissolved, ultra-pure clinopyroxene and orthopyroxene separates. Moreover, in situ analyses of olivine and spinel show systematically lower incompatible-element abundances than the solution chemistry analyses, reflecting impurities in the mineral separates used in the latter analyses. These impurities may be in the form of μg quantities of other minerals such as clinopyroxene, or thin films of glass in cracks and on grain boundaries [see item (2), below].

(2) Mass balance is achieved for the highly incompatible trace elements only with inclusion of data for rare precursor amphibole, now present as pockets of alkali-, alumina- and silica-rich glass containing euhedral olivine, clinopyroxene, and spinel daughter crystals. The glass in these pockets is enriched in incompatible trace elements, particularly Ba, Nb and Ta, reflecting the preferential partitioning of these elements into amphibole at upper-mantle conditions.

(3) With inclusion of the former amphibole, the non-volatile incompatible elements are quantitatively accounted for in the mineral phases under upper-mantle conditions — no significant concentrations of these elements are on grain boundaries or in fluid inclusions, nor are exotic accessory minerals required hosts for elements such as Nb and Ta.

(4) Orthopyroxene–clinopyroxene partition coefficients for incompatible elements measured in this study are the same in the two samples (except for Ti), implying that bulk composition plays little role in controlling subsolidus partitioning. However, the large range in literature values of $D^{opx/cpx}$ for many incompatible elements demonstrates that T and P, and possibly phase assemblage have significant effects on subsolidus partitioning, suggesting caution in applying these D-values to infer crystal–liquid D-values.

Acknowledgements

This work has been made possible by the assistance and technical expertise of Mike Shelley, Les Kinsley, Nick Ware, Graeme Mortimer and Richard Rudowski. We thank Kim Patrick for performing some of the electron probe analyses. Dimitri Ionov kindly shared some of his unpublished data. Heinz-Günter Stosch, Fred Frey, Gilles Chazot and two anonymous reviewers are thanked for their thorough and critical evaluation of the manuscript. Finally, we thank Steve Richardson for his paleogeotechnical skills in coming up with unpublished major-element data for some samples. RLR and WFM acknowledge the support of the ANU in the initial stages of this research and the NSF (grant numbers EAR 95-06510 to RLR and EAR 95-06517 to WFM) in the later stages of the work. SME has undertaken this work through support from an ARC Postdoctoral Fellowship and an ARC Research Fellowship. ***[CH]***

Appendix A

The major- and incompatible trace-element compositions of former amphibole were estimated by combining the glass compositions with those of the secondary phases according to the phase proportions for the amphibole breakdown reaction reported by Chazot et al. [21], see Table 6. For this calculation, the trace-element composition of the secondary clinopyroxene was estimated from cpx–melt partition coefficients (the minerals were too small to

measure directly); the trace-element contributions of olivine and spinel are assumed to be zero. Concentrations of most highly incompatible trace elements in the reconstituted amphibole are simply ~40% of the measured glass concentrations.

References

[1] F.A. Frey, Rare earth abundances in a high-temperature peridotite intrusion, Geochim. Cosmochim. Acta 33 (1969) 1429–1447.

[2] H. Nagasawa, H. Wakita, H. Higuchi, N. Onuma, Rare earths in peridotite nodules: an explanation of the genetic relationships between basalt and peridotite nodules, Earth Planet. Sci. Lett. 5 (1969) 377–381.

[3] F.A. Frey, D.H. Green, The mineralogy, geochemistry and origin of lherzolite inclusions in Victorian basanites, Geochim. Cosmochim. Acta 38 (1974) 1023–1059.

[4] N. Shimizu, Rare earth elements in garnets and clinopyroxenes from garnet lherzolite nodules in kimberlites, Earth Planet. Sci. Lett. 25 (1975) 26–32.

[5] N. Shimizu, S.H. Richardson, Trace element abundance patterns of garnet inclusions in peridotite-suite diamonds, Geochim. Cosmochim. Acta 51 (1987) 755–758.

[6] N. Shimizu, C.J. Allègre, Geochemistry of transition elements in garnet lherzolite nodules in kimberlites, Contrib. Mineral. Petrol. 67 (1978) 41–50.

[7] K.T.M. Johnson, H.J.B. Dick, N. Shimizu, Melting in the oceanic upper mantle: an ion microprobe study of diopsides in abyssal peridotites, J. Geophys. Res. 95 (1990) 2661–2678.

[8] V.J.M. Salters, N. Shimizu, World-wide occurrence of HFSE-depleted mantle, Geochim. Cosmochim. Acta 52 (1988) 2177–2182.

[9] N. Shimizu, J.J. Gurney, R. Moore, Trace element geochemistry of garnet inclusions in diamonds from the Finsch and Koffiefontein kimberlite pipes, 28th Int. Geol. Congr., Extend. Abstr. Workshop on Diamonds, 1989, pp. 100–101.

[10] W.F. McDonough, H.-G. Stosch, N. Ware, Distribution of titanium and the rare earth elements between peridotitic minerals, Contrib. Mineral. Petrol. 110 (1992) 321–328.

[11] E. Rampone, G.B. Piccardo, R. Vannucci, P. Bottazzi, L. Ottolini, Subsolidus reactions monitored by trace element partitioning: the spinel- to plagioclase-facies transition in mantle peridotites, Contrib. Mineral. Petrol. 115 (1993) 1–17.

[12] J.-L. Bodinier, C. Merlet, R.M. Bedini, F. Siemen, M. Ramaidi, C.J. Garrido, Distribution of niobium and tantalum and other highly incompatible trace elements in the lithospheric mantle: the spinel paradox, Geochim. Cosmochim. Acta 60 (1996) 545–550.

[13] E.J. Dasch, D.H. Green, Strontium isotope geochemistry of lherzolite inclusions and host basaltic rocks, Victoria, Australia, Am. J. Sci. 275 (1975) 461–469.

[14] D. Canil, H.S.C. O'Neill, D.G. Pearson, R.L. Rudnick, W.F. McDonough, D.A. Carswell, Ferric iron in peridotites and mantle oxidation states, Earth Planet. Sci. Lett. 123 (1994) 205–220.

[15] W.F. McDonough, M.T. McCulloch, The southeast Australian lithospheric mantle: isotopic and geochemical constraints on its growth and evolution, Earth Planet. Sci. Lett. 86 (1987) 327–340.

[16] W.F. McDonough, F.A. Frey, REE in upper mantle rocks, in: B. Lipin, G.R. McKay (Eds.), Geochemistry and Mineralogy of Rare Earth Elements, Mineral. Soc. Am., Rev. Mineral. 21 (1989) 99–145.

[17] P.R.A. Wells, Pyroxene thermometry in simple and complex systems, Contrib. Mineral. Petrol. 62 (1977) 129–139.

[18] G.P. Brey, T. Köhler, Geothermobarometry in four-phase lherzolites, II. New thermobarometers, and practical assessment of existing thermobarometers, J. Petrol. 31 (1990) 1353–1378.

[19] G.M. Yaxley, V. Kamenetsky, D.H. Green, T.J. Falloon, Glasses in mantle xenoliths from western Victoria, Australia and their relevance to mantle processes, Earth Planet. Sci. Lett. 148 (1997) 433–446.

[20] H.-G. Stosch, H.A. Seck, Geochemistry and mineralogy of two spinel peridotite suites from Dreiser Weiher, West Germany, Geochim. Cosmochim. Acta 44 (1980) 457–470.

[21] G. Chazot, M.A. Menzies, B. Harte, Determination of partition coefficients between apatite, clinopyroxene, amphibole and melt in natural spinel lherzolites from Yemen: implications for wet melting of the lithospheric mantle, Geochim. Cosmochim. Acta 60 (1996) 423–437.

[22] P. Schiano, R. Clocchiatti, Worldwide occurrence of silica-rich melts in sub-continental and sub-oceanic mantle minerals, Nature (London) 368 (1994) 621–624.

[23] N.G. Ware, Combined energy-dispersive–wavelength-dispersive quantitative electron microprobe analysis, X-Ray Spectrom. 20 (1991) 73–79.

[24] S.M. Eggins, J.D. Woodhead, L. Kinsley, G.E. Mortimer, P. Sylvester, M.T. McCulloch, J.M. Hergt, M.R. Handler, A simple method for the precise determination of ≥40 trace elements in geological samples by ICP–MS using enriched isotope internal standardisation, Chem. Geol. 134 (1997) 311–326.

[25] S.M. Eggins, L.P.J. Kinsley, J.M. Shelley, Deposition and element fractionation processes during atmospheric pressure laser sampling for analysis by ICPMS, Surface Sci. (1997, submitted).

[26] S.M. Eggins, R.R. Loucks, M.T. McCulloch, P. Sylvester, L. Kinsley, M.J.R. Shelley, In-situ determination of 40 or more trace elements in geological standards by laser ablation ICP–MS, Chem. Geol. (1997, in prep.).

[27] H.P. Longerich, S.E. Jackson, D. Günther, Laser ablation inductively coupled plasma mass spectrometric transient signal data acquisition and analyte concentration calculation, J. Anal. At. Spectrosc. 11 (1996) 899–904.

[28] W.F. McDonough, S.-s. Sun, The composition of the Earth, Chem. Geol. 120 (1995) 223–253.

[29] H.-G. Stosch, Rare earth element partitioning between minerals from anhydrous spinel peridotite xenoliths, Geochim. Cosmochim. Acta 46 (1982) 793–811.

[30] K.P. Jochum, H.M. Seufert, B. Spettel, H. Palme, The solar-system abundances of Na, Ta, and Y, and the relative abundances of refractory lithophile elements in differentiated planetary bodies, Geochim. Cosmochim. Acta 50 (1986) 1173–1183.
[31] A. Zindler, E. Jagoutz, Mantle cryptology, Geochim. Cosmochim. Acta 52 (1988) 319–333.
[32] D. Ionov, Distribution and residence of lithophile trace elements in minerals of garnet and spinel peridotites: an ICP–MS study, J. Conf. Abstr. 1 (1996) 278.
[33] M. Sun, R. Kerrich, Rare earth element and high field strength element characteristics of whole rocks and mineral separates of ultramafic nodules in Cenozoic volcanic vents of southeastern British Columbia, Canada, Geochim. Cosmochim. Acta 59 (1995) 4863–4874.
[34] R.L. Rudnick, Making continental crust, Nature (London) 378 (1995) 571–578.
[35] D.A. Ionov, A.W. Hofmann, Nb–Ta-rich mantle amphiboles and micas: implications for subduction-related metasomatic trace element fractionations, Earth Planet. Sci. Lett. 131 (1995) 341–356.
[36] G. Witt-Eickschen, B. Harte, Distribution of trace elements between amphibole and clinopyroxene from mantle peridotite of the Eifel (western Germany): an ion-microprobe study, Chem. Geol. 117 (1994) 235–250.
[37] O. Vaselli, H. Downes, M. Thirlwall, G. Dobosi, N. Coradossi, I. Seghedi, A. Szakacs, R. Vannucci, Ultramafic xenoliths in Plio-Pleistocene alkali basalts from the eastern Transylvanian basin: depleted mantle enriched by vein metasomatism, J. Petrol. 36 (1995) 23–53.
[38] R. Vanucci, G.B. Piccardo, G. Rivalenti, A. Zanetti, E. Rampone, L. Ottolini, R. Oberti, M. Mazzucchelli, P. Bottazzi, Origin of LREE-depleted amphiboles in the subcontinental mantle, Geochim. Cosmochim. Acta 59 (1995) 1763–1771.
[39] D.A. Ionov, V.S. Prikhod'ko, S.Y. O'Reilly, Peridotite xenoliths in alkali basalts from the Sikhote-Alin, southeastern Siberia, Russia: trace-element signatures of mantle beneath a convergent continental margin, Chem. Geol. 120 (1995) 275–294.
[40] P.B. Kelemen, N. Shimizu, T. Dunn, Relative depletion of niobium in some arc magmas and the continental crust: partitioning of K, Nb, La and Ce during melt/rock reaction in the upper mantle, Earth Planet. Sci. Lett. 120 (1993) 111–126.
[41] R.L. Hervig, J.V. Smith, J.B. Dawson, Lherzolite xenoliths in kimberlites and basalts: petrogenetic and crystallochemical significance of some minor and trace elements in olivine, pyroxenes, garnet and spinel, Trans. R. Soc. Edinburgh: Earth Sci. 77 (1986) 181–201.
[42] J.-L. Bodinier, C. Dupuy, J. Dostal, C. Merlet, Distribution of trace transition elements in olivine and pyroxenes form ultramafic xenoliths: application of microprobe analysis, Am. Mineral. 72 (1987) 902–913.
[43] E. Hauri, N. Shimizu, J.J. Dieu, S.R. Hart, Evidence for hotspot-related carbonatite metasomatism in the oceanic upper mantle, Nature (London) 365 (1993) 221–227.
[44] G.A. McKay, Partitioning of rare earth elements between major silicate minerals and basaltic melts, in: B.R. Lipin, G.A. McKay (Eds.), Geochemistry and Mineralogy of Rare Earth Elements, Mineral. Soc. Am., Rev. Mineral. 21 (1989) 45–77.
[45] H.-G. Stosch, Sc, Cr, Co and Ni partitioning between minerals from spinel peridotite xenoliths, Contrib. Mineral. Petrol. 78 (1981) 166–174.